Monthly Notices
of the
ROYAL ASTRONOMICAL SOCIETY

MNRAS **481,** 793–805 (2018)
Advance Access publication 2018 August 18

doi:10.1093/mnras/sty2239

A newly identified emission-line region around P Cygni

Misaki Mizumoto,[1,2★] Naoto Kobayashi,[3,4,5] Satoshi Hamano,[5] Yuji Ikeda,[5,6] Sohei Kondo,[5] Hiroaki Sameshima,[5] Noriyuki Matsunaga,[1,5] Kei Fukue,[5] Chikako Yasui,[7] Natsuko Izumi,[7] Hideyo Kawakita,[5,8] Kenshi Nakanishi,[5,8] Tetsuya Nakaoka,[5,8] Shogo Otsubo[5,8] and Hiroyuki Maehara[9]

[1]*Department of Astronomy, Graduate School of Science, The University of Tokyo, Hongo, Bunkyo-ku, Tokyo 113-0033, Japan*
[2]*Centre for Extragalactic Astronomy, Department of Physics, University of Durham, South Road, Durham DH1 3LE, UK*
[3]*Kiso Observatory, Institute of Astronomy, School of Science, The University of Tokyo, Mitake, Kiso-machi, Kiso-gun, Nagano 397-0101, Japan*
[4]*Institute of Astronomy, Graduate School of Science, The University of Tokyo, Osawa, Mitaka, Tokyo 181-0015, Japan*
[5]*Laboratory of IR High-resolution Spectroscopy (LIH), Koyama Astronomical Observatory, Kyoto Sangyo University, Motoyama, Kamigamo, Kita-Ku, Kyoto 603-8555, Japan*
[6]*Photocoding, Iwakura-Kita-Ikedacho, Sakyo-Ku, Kyoto 606-0004, Japan*
[7]*National Astronomical Observatory of Japan, Osawa, Mitaka, Tokyo 181-8588, Japan*
[8]*Department of Physics, Faculty of Science, Kyoto Sangyo University, Motoyama, Kamigamo, Kita-ku, Kyoto 603-8555, Japan*
[9]*Okayama Astrophysical Observatory, National Astronomical Observatory of Japan, Honjo, Kamogata, Asakuchi, Okayama 719-0232, Japan*

Accepted 2018 August 13. Received 2018 August 13; in original form 2018 March 12

ABSTRACT

We present a high-resolution ($R \simeq 20\ 000$) near-infrared (9100–13 500Å) long-slit spectrum of P Cygni obtained with the newly commissioned WINERED spectrograph in Japan. In the obtained spectrum, we have found that the velocity profiles of the [Fe II] emission lines are resolved into two peaks at a velocity of $\simeq$220 km s^{-1} with a moderate dip in between and with additional sub-peaks at $\simeq\pm$100 km s^{-1}. The sub-peak component is confirmed with the long-slit echellogram to originate in the known shell with a radius of $\simeq$10 arcsec, which was originally created by the outburst in 1600 AD. On the other hand, the $\simeq$220 km s^{-1} component, which dominates the [Fe II] flux from P Cygni, is found to be concentrated closer to the central star with an apparent spatial extent of $\simeq$3 arcsec. The extent is much larger than the compact (<0.1 arcsec) regions traced with hydrogen, helium, and metal permitted lines. The velocity, estimated mass, and dynamical time of the extended emission-line region suggest that the region is an outer part of the stellar wind region. We suggest that the newly identified emission-line region may trace a reverse shock due to the stellar wind overtaking the outburst shell.

Key words: stars: individual (P Cygni) – stars: mass-loss – stars: winds, outflows.

1 INTRODUCTION

Luminous blue variable (LBV) stars are believed to have evolved from high-mass main-sequence stars and to become eventually Wolf–Rayet stars after various magnitudes of mass-loss (e.g. Langer et al. 1994; Meynet et al. 2011; Smith 2014; and references therein). Circumstellar nebulae around LBV stars provide essential clues for mass-loss events (e.g. Najarro, Hillier & Stahl 1997b) and evolutionary process of LBV stars (e.g. Smith et al. 2011; Weis 2011). Steady mass-loss events create emission photospheres or shells around stars (e.g. Lamers, Korevaar & Cassatella 1985), whereas flash mass-loss events, which are often called 'eruptions' or 'outbursts', create emission shells as those seen in P Cygni and η Carinae (e.g. Lamers 1986; Humphreys, Davidson & Smith 1999; Ishibashi et al. 2003; Smith & Hartigan 2006). Thus, the structure and kinematics of the LBV nebulae give us important clues about the mass-loss events.

Infrared (IR) [Fe II] lines are a powerful tool for investigating the structure and physical mechanisms of the LBV mass-loss events (Smith 2002a). Bright IR [Fe II] lines are typically detected towards shock-excited objects or outflowing objects, such as supernova remnants, massive stars, and low-mass young stellar objects (e.g. Meaburn et al. 2000; Smith 2001, 2002a; Hartigan, Raymond & Pierson 2004; Lee et al. 2009; Shinn et al. 2013), and are detected in all the observed LBVs with near-IR (NIR) spectroscopy (Smith 2002a). Because the LBV nebulae are optically thin at the IR wavelength region, IR observations are key tools to study the

★ E-mail: misaki.mizumoto@durham.ac.uk

circumstellar nebulae of LBVs (e.g. Artigau et al. 2011; Clark et al. 2011; Gvaramadze et al. 2012). For example, NIR observations of η Carinae clearly resolve the emission components from different areas (Smith 2002b, 2006).

Barlow et al. (1994) found a circular nebula around P Cygni with an angular radius of ∼11 arcsec and an expansion velocity of 140 km s^{-1} using the optical [N II] λ6584 line. Smith & Hartigan (2006) (hereafter SH06) deeply investigated this nebula using the NIR [Fe II] λ16 440 line, and concluded that this nebula with a shell-like structure with a radius of ∼8−10 arcsec was ejected by the 1600-AD outburst. Other circumstellar nebulae outside of the 1600-AD outburst shell have also been studied (e.g. Meaburn et al. 1996, 2000). In addition, the [Fe II] emission of P Cygni inside the 1600-AD outburst shell has also been investigated and found to be created in the region of $R \gtrsim 100R_*$, where R_* is the radius of P Cygni (=76 ± 14 R$_\odot$; Lamers, de Groot & Cassatella 1983), based on the line ratio and/or the velocity width of the optical [Fe II] emission lines (e.g. Israelyan & de Groot 1991; Stahl et al. 1991; Markova & de Groot 1997). Markova (2000) suggested that the forbidden lines in P Cygni originate at $\simeq 100R_*$, where the wind has reached its terminal velocity. However, to our surprise, the upper limit for the radius of the [Fe II] emission region has not been explicitly constrained. Arcidiacono et al. (2014) shows the [Fe II] λ16440 image of P Cygni nebula with high angular resolution by adaptive-optics observations, but the inner structure within 3 arcsec is unclear because they masked the region.

Here, we observed P Cygni with a newly developed high-resolution ($R \simeq 20\ 000$) NIR (9100–13 500 Å) echelle 'WINERED' spectrograph. P Cygni is the nearest LBV star at a distance of 1.7 kpc (Najarro et al. 1997b) and thus the best target to study mass-loss events in LBVs. The range of the studied wavelengths, 9100–13 500 Å, falls between the optical and IR wavelengths and has been relatively poorly studied in astronomy. However, this 'niche' wavelength range is rich in various types of emission lines, yet is contaminated less with background lines than optical wavelengths.

In this paper, we first describe the WINERED spectrograph and the observation in Section 2. In Section 3, we show that the velocity profiles of the NIR [Fe II] lines have a clear 'double-peak', which have been considered as 'flat-topped' in the past studies, and constrain the spatial extent of the [Fe II] emission region. Finally, we discuss the origin of the extended region of the [Fe II] emission in Section 4.

2 OBSERVATIONS AND DATA REDUCTION

We obtained the spectrum of P Cygni on 2014 September 20 with the NIR high-resolution spectrograph WINERED (Ikeda et al. 2016), mounted on the F/10 Nasmyth focus of the Araki 1.3 m telescope at Koyama Astronomical Observatory, Japan (Yoshikawa et al. 2012). WINERED uses a 1.7 μm cut-off 2048 × 2048 HAWAII-2RG array with a pixel scale of 0.8 arcsec pixel^{-1}, covering the wavelength range of 9100–13 500Å simultaneously. Fig. 1 shows the slit position relative to the central star of P Cygni. We used a long slit with a length of 48 arcsec, oriented along PA $\simeq 37^\circ$. The slit width is 1.6 arcsec (2 pixel), which provides the maximum spectral resolving power of $R \simeq 28\ 300$ or $\Delta v \simeq 11$ km s^{-1}. However, our observed spectrum has a lower spectral resolution of $R \simeq 20\ 000$ ($\Delta v \simeq 15$ km s^{-1}) due to the optical setting during the observing period. The exposure time was 150 s frame^{-1}, which was long enough to make some strong H I and He I lines saturated in the obtained spectra. We observed P Cygni eight times and combined all the frames; thus, the total exposure time was 1200 s. The one-dimensional spectrum was created, using the data within the slit-length of ≃10 arcsec. The obtained S/N (signal-to-noise ratio) was 130. The wavelength was calibrated using the spectrum of a Th-Ar lamp in front of the slit. The uncertainty of the central velocities of the lines was smaller than 1 km s^{-1}. For the telluric-absorption correction, we used the spectrum of the spectrometric standard star 28 Cet, obtained at the similar airmass to that in our observations. The sky conditions were photometric and the seeing was relatively good for the site [full width at half-maximum (FWHM) ∼ 4 arcsec].

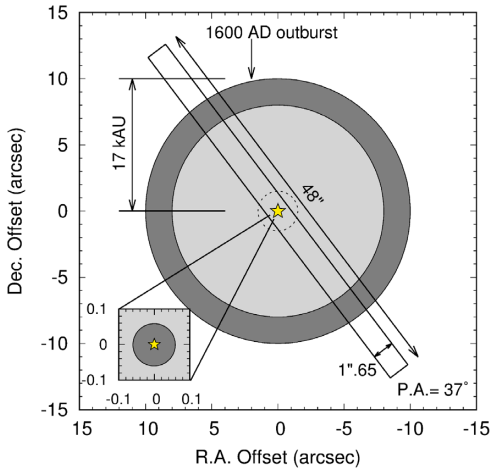

Figure 1. The position and PA of the slit for the WINERED observation of P Cygni and its nebula. The horizontal and vertical axes show the offsets in the RA and Dec., respectively, in arcsec from the position of P Cygni, which is denoted as the star symbol at the centre. The tilted and slender rectangle shows the position of the slit on the sky. The dark-grey ring with radii of 8–10 arcsec illustrates the 1600-AD outburst shell (SH06). The dark-grey filled circle with a radius of ∼0.06 arcsec in the inset illustrates the extent of the steady mass-loss wind region (∼100 au). The dotted line is a circle with a diameter of 2.9 arcsec (=4.9 kau), which demonstrates the extent of the [FeII] emission-line region we have discovered (see the main text in Section 3.2).

3 RESULTS

3.1 Velocity profiles

We found 90 emission lines in the whole spectrum of P Cygni. Table 1 and Fig. 2 show the linelist and the whole spectrum we obtained. We used VALD3 (Kupka et al. 1999) when identifying the atomic lines. Fig. 3 shows some characteristic velocity profiles of emission lines. The so-called P Cygni profiles (Fig. 3a) are clearly seen in H I and He I lines with a terminal velocity of −220 km s^{-1}, which originates in the optically thick and steady mass-loss wind region around the star with a radius of ∼100 R_* (e.g. Lamers et al. 1985; see also the inset in Fig. 1). Rounded profiles (Fig. 3b) with a velocity of 180 km s^{-1} are visible in metal permitted lines, such as O I, Mg II, and Fe II, which are formed in the optically thin and steady mass-loss wind region with a radius of $\lesssim$100 R_* (e.g. Najarro et al. 1997b; Markova & de Groot 1997; Rossi, Muratorio & Viotti 2001). The central velocity of Fe II λ10504, −28± 1 km s^{-1}, is consistent with the known systemic velocity of P Cygni (e.g. −22 km s^{-1} in Barlow et al. 1994 and Markova & de Groot 1997, −27 km s^{-1} in Meaburn 2001, and −29 km s^{-1} in Stahl et al. 1993). The interpretation of 'P Cygni' and 'rounded' profiles is also consistent with those in previous studies.

Table 1. Line list.

Line	λ_{vac} (Å)	λ_{air} (Å)	Transition	Rank[a]	Ref.[b]	Line	λ_{vac} (Å)	λ_{air} (Å)	Transition	Rank	Ref.
Mg II	9220.7799	9218.250	$^2S_1 - {}^2P_3$	B		Fe II	10549.378	10546.488	$e^6D_9 - y^6F_{11}$	A	1
Pa ζ	9231.5498	9229.017		A	4	Fe II	10638.765	10635.851	$e^4G_5 - {}^2F_7$	B	
Mg II	9246.8019	9244.265	$^2S_1 - {}^2P_1$	B		He I	10670.898	10667.975	$^3P_0 - {}^3S_2$	A	1
Fe II?	9264.4448	9261.903	$^2[3]_7 - {}^4F_5$	X		O I	10732.881	10729.941	$^5P_6 - {}^5S_4$	B	
Ni II?	9268.7769	9266.234	$^2F_5 - {}^2[3]_7$	X		He I	10832.055	10829.088	$^3S_2 - {}^3P_0$	A	1, 3, 4
Fe II	9299.4709	9296.920	$e^4D_5 - {}^4D_5$	A	4	Fe II	10865.628	10862.652	$z^4F_5 - b^4G_7$	A	1, 3, 4
Fe II?	9390.509	9387.933	$^4D_7 - {}^4F_5$	X		He I	10916.022	10913.033	$^3D_6 - {}^3F_8$	A	3, 4
Fe II	9408.653	9406.072	$u^4F_5 - {}^4G_5$	A	4	He I	10920.088	10917.098	$^1D_4 - {}^1F_6$	A	1
Fe II?	9415.1861	9412.604	$t^2F_5 - {}^2G_7$	X		Pa γ	10941.089	10938.093		A	1, 3, 4
He I	9466.1383	9463.542	$^3S_2 - {}^3P_0$	A	4	Mg II	10954.778	10951.778	$^2D_3 - {}^2P_1$	A	1
He I	9519.2437	9516.633	$^3P_4 - {}^3D_6$	A	4	Fe II?	10969.029	10966.025	$^4H_{11} - {}^2H_{11}$	X	
He I	9531.8841	9529.270	$^1D_4 - {}^1F_6$	B		He I?	10999.573	10996.561	$^3D_6 - {}^3P_4$	X	
Pa ε	9548.5917	9545.973		A	4	He I?	11016.086	11013.070	$^1S_0 - {}^1P_2$	X	
He I	9606.0522	9603.418	$^1S_0 - {}^1P_2$	B		He I	11048.028	11045.003	$^1P_2 - {}^1D_4$	A	1
He I	9628.2812	9625.641	$^1P_2 - {}^1D_4$	B		Fe II	11128.64	11125.593	$z^4F_3 - b^4G_5$	A	4
C I	9661.0834	9658.434	$^3P_4 - {}^3S_2$	A	4	O I	11289.408	11286.317	$^3P_2 - {}^3D_4$	A	3, 4
He I?	9684.8466	9682.191	$^1P_2 - {}^1S_0$	X		Mg II	11754.846	11751.629	$^2F_7 - {}^2D_5$	B	
He I	9705.5312	9702.870	$^3P_0 - {}^3S_2$	A	4	Fe II?	11831.826	11828.588	$^6D_7 - {}^6D_5$	X	
Fe I?	9801.9266	9799.239	$w^5D_6 - g^7D_8$	X		Fe II?	11842.663	11839.422	$^4G_5 - {}^2[2]_3$	X	
Fe II	9868.7106	9866.005	$^2[1]_3 - {}^2[3]_5$	B		Fe II?	11883.959	11880.707	$^4H_{11} - {}^4I_{11}$	X	
Fe I	9887.4294	9884.719	$^2[2]_3 - {}^2[3]_5$	B		C I	11899.006	11895.750	$^3D_6 - {}^3P_4$	A	4
Fe I	9893.3941	9890.682	$^2[5]_9 - {}^2[5]_9$	B		Fe II	11954.218	11950.947	$^2P_3 - {}^2[1]_3$	B	
Fe I	9905.3288	9902.614	$e^5F_4 - {}^3D_4$	B		He I	11972.336	11969.060	$^3P_4 - {}^3D_6$	A	3, 4
Fe II	9934.3666	9931.643	$f^4G_9 - {}^2[5]_9$	B		Fe II?	12329.941	12326.568	$^6S_5 - {}^2[3]_5$	X	
Fe II	9959.0524	9956.323	$z^4F_9 - b^4G_9$	A	4	Fe II?	12385.369	12381.981	$^2G_7 - {}^4G_9$	X	
N I	9971.2432	9968.510	$^4D_5 - {}^4P_3$	B		Fe II	12467.78	12464.370	$^6P_5 - {}^4S_3$	A	4
Fe I	9984.6167	9981.880	$n^7D_6 - {}^2[5/2]_6$	B		Fe I	12498.742	12495.323	$h^5D_8 - {}^5F_{10}$	B	
Fe II	10000.079	9997.338	$^4P_3 - {}^6D_5$	A	2	He I	12530.778	12527.350	$^3S_2 - {}^3P_0$	A	3, 4
Al II?	10020.14	10017.394	$^1G_8 - {}^1F_6$	X		[Fe II]	12570.206	12566.768	$^a6D_9 - a^4D_7$	A	3, 4
He I	10030.465	10027.716	$^3D_6 - {}^3F_8$	A	2, 4	Fe I	12603.308	12599.861	$e^7F_4 - {}^2[7/2]_6$	B	
He I	10033.904	10031.154	$^1D_4 - {}^1F_6$	A	2, 4	Fe II?	12618.98	12615.528	$^4G_7 - {}^2[3]_7$	X	
Fe I?	10037.351	10034.600	$e^5F_4 - {}^3P_4$	X		[Fe II]	12706.91	12703.435	$a^6D_1 - a^4D_1$	A	3, 4
Pa δ	10052.128	10049.373		A	2, 4	Fe II?	12771.147	12767.654	$^4H_9 - {}^2[5]_{11}$	X	
C I	10067.629	10064.870	$^3P_0 - {}^3P_2$	B		He I	12788.483	12784.985	$^3D_6 - {}^3F_8$	A (New)	
He I?	10074.809	10072.048	$^3D_6 - {}^3P_4$	X		He I	12794.064	12790.565	$^1D_4 - {}^1F_6$	A (New)	
Mg II	10094.862	10092.095	$^2F_5 - {}^2G_7$	B		Fe II?	12807.544	12804.041	$e^4G_5 - u^4F_7$	X	
Al II	10110.212	10107.441	$^3D_4 - {}^3P_2$	A	2	Pa β	12821.584	12818.077		A	3, 4
N I	10117.413	10114.640	$^4D_7 - {}^4F_9$	A	2, 4	He I	12849.449	12845.935	$^3P_4 - {}^3S_2$	A (New)	
He II?	10126.367	10123.592		X		Fe II?	12864.03	12860.512	$^2H_9 - {}^2[4]_7$	X	
He I	10141.214	10138.435	$^1P_2 - {}^1D_4$	A	2	Fe II?	12893.295	12889.769	$^4H_7 - {}^2[4]_9$	X	
Fe II	10176.303	10173.514	$z^4D_7 - b^4G_9$	A	4	[Fe II]	12946.204	12942.664	$a^6D_5 - a^4D_5$	A	3, 4
He I	10314.044	10311.218	$^3P_4 - {}^3D_2$	A	3, 4	He I	12971.986	12968.439	$^1P_2 - {}^1D_4$	A (New)	
Fe II	10436.446	10433.587	$w^4G_{11} - {}^4G_9$	B		He I	12988.434	12984.882	$^3D_6 - {}^3P_4$	A (New)	
Fe II	10504.38	10501.502	$z^4F_7 - b^4G_9$	A	3, 4	O I	13168.732	13165.131	$^3P_0 - {}^3S_2$	A	3, 4
Fe II	10525.135	10522.252	$^2[2]_3 - {}^6D_1$	B		[Fe II]	13209.111	13205.499	$a^6D_7 - a^4D_7$	A	3, 4

[a](A): (Newly) identified; (B): Probably identified; (X): Detected but not identified; possible candidates are shown.
[b]References: 1: Groh, Damineli & Jablonski (2007), 2: Rossi et al. (2001), 3: SH06, 4: Hamann et al. (1994). Note that the linelist in [4] is for η Carinae.

We have clearly resolved for the first time each of the [Fe II] emission lines in the obtained spectrum into two peaks, or a 'double-peak' profile, with a velocity of $\simeq$220 km s^{-1} (Fig. 3c). Several optical/IR [Fe II] lines were previously detected in this object, yet none of the lines have been resolved into multiple peaks, even though the observed profiles of the lines were known to be somewhat broad and probably to have a flat top at the (single) peak. Markova (2000) proposed the interpretation that these 'flat-topped' profiles are formed in the mass-loss wind region of a constant expansion velocity at a radius of $\sim$100 au. However, the compact emission region with a constant expansion velocity cannot generate such a 'double-peak' profile as we obtained. Figs 3(c)–(f) show velocity profiles of all the four [Fe II] lines obtained in this observation. The [Fe II] λ12570 ($a^4D_7 - a^6D_9$) line is the strongest [Fe II] line in the observed range of wavelengths, and clearly shows the 'double-peak' profile at $v \simeq \pm$220 km s^{-1} and sub-peaks at $v \simeq \pm$100 km s^{-1}. The [Fe II] λ12707 ($a^4D_1 - a^6D_1$) line was detected, but too faint to evaluate the velocity profile quantitatively. The [Fe II] λ12946 ($a^4D_5 - a^6D_5$) line was also detected, but its red wing is slightly contaminated with the adjacent He I λ12972. Although [Fe II] λ13209 ($a^4D_7 - a^6D_7$) is affected by residuals of a strong telluric absorption line, the velocity profile shows the relatively clear 'double-peak' profile in the same way as that of [Fe II] λ12570.

3.2 Spatial extent of [Fe II]

Fig. 4 shows the echelle image around the [Fe II] λ12570 line. The 1600-AD outburst shell, which has an expansion velocity

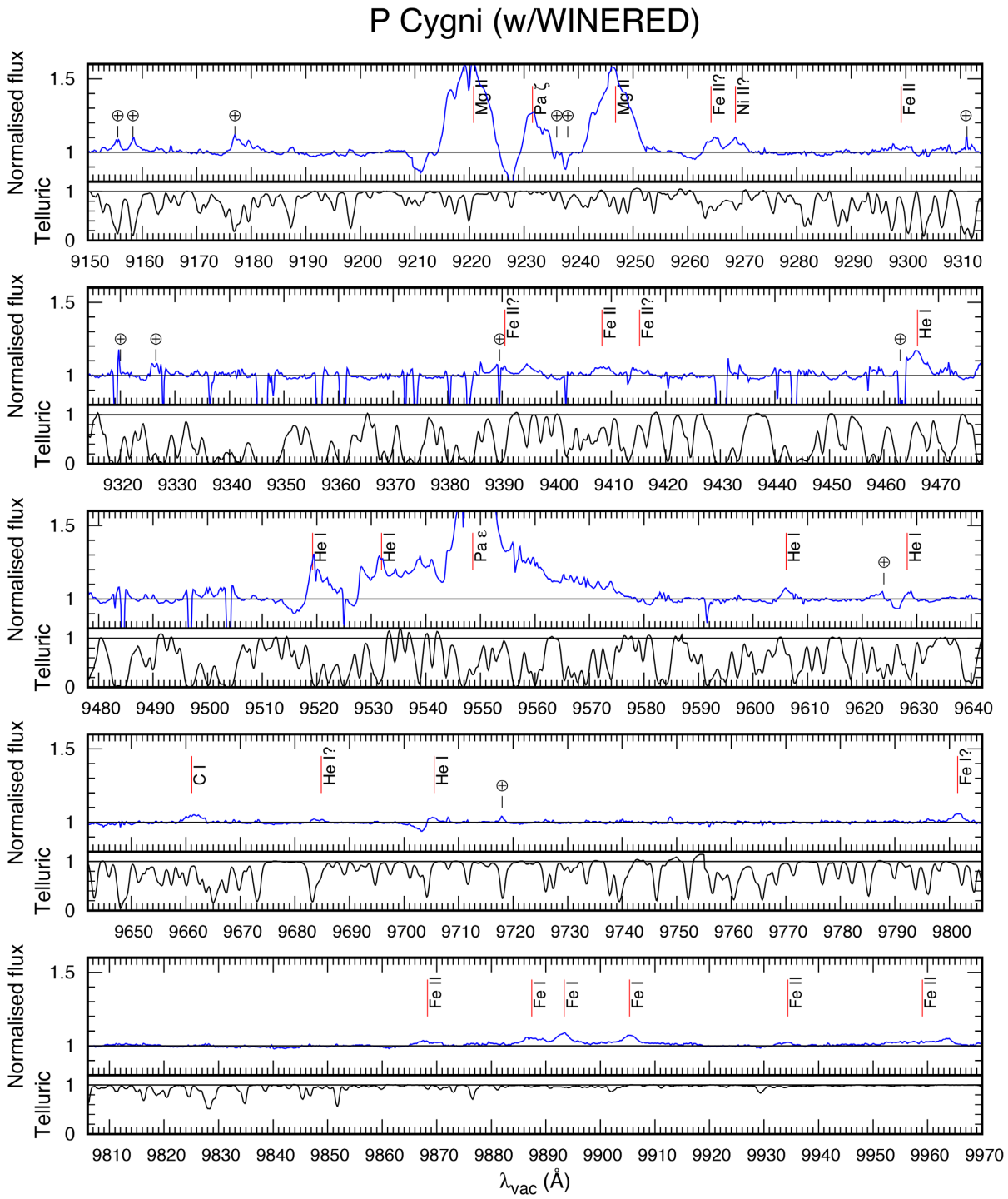

Figure 2. The WINERED spectrum of P Cygni and its nebula in the slit area shown in Fig. 1. The horizontal axis shows the wavelength in vacuum. The telluric absorption is corrected using the spectrum of the standard star, which is shown in the bottom of each plot after removing the intrinsic stellar absorption lines and being normalized. The vertical red lines above the spectrum show emission lines. The other spike-like emission features as well as a group of sharp absorption features in the bad atmospheric transmission region (especially 9310–9800 Å and 11120–11750 Å) are due to incomplete telluric correction. The ⊕ symbols show the part where telluric absorptions are not fully corrected because of their heavy absorption.

of $\simeq$140 km s^{-1} and a radius of 8−10 arcsec, is apparent in the echelle image (n.b., this image is in the same configuration as in fig. 5 of SH06 around [Fe II] λ16440). This shell is responsible to create the sub-peaks at $v \simeq \pm 100$ km s^{-1} in the projected spectrum (Section 3.1, see also the green dotted lines in Fig. 4.) However, the spatial extent of the stronger emission with double peak at $v \simeq \pm 220$ km s^{-1} is unclear in the upper panel of Fig. 4, suggesting that it has a spatially smaller region than the outburst shell and that it is hindered under the very strong continuum.

In order to study the spatial extent of the [Fe II] emission component with $v \simeq \pm 220$ km s^{-1} double peak, we subtracted the model continuum on the echelle image. First, we extracted 52

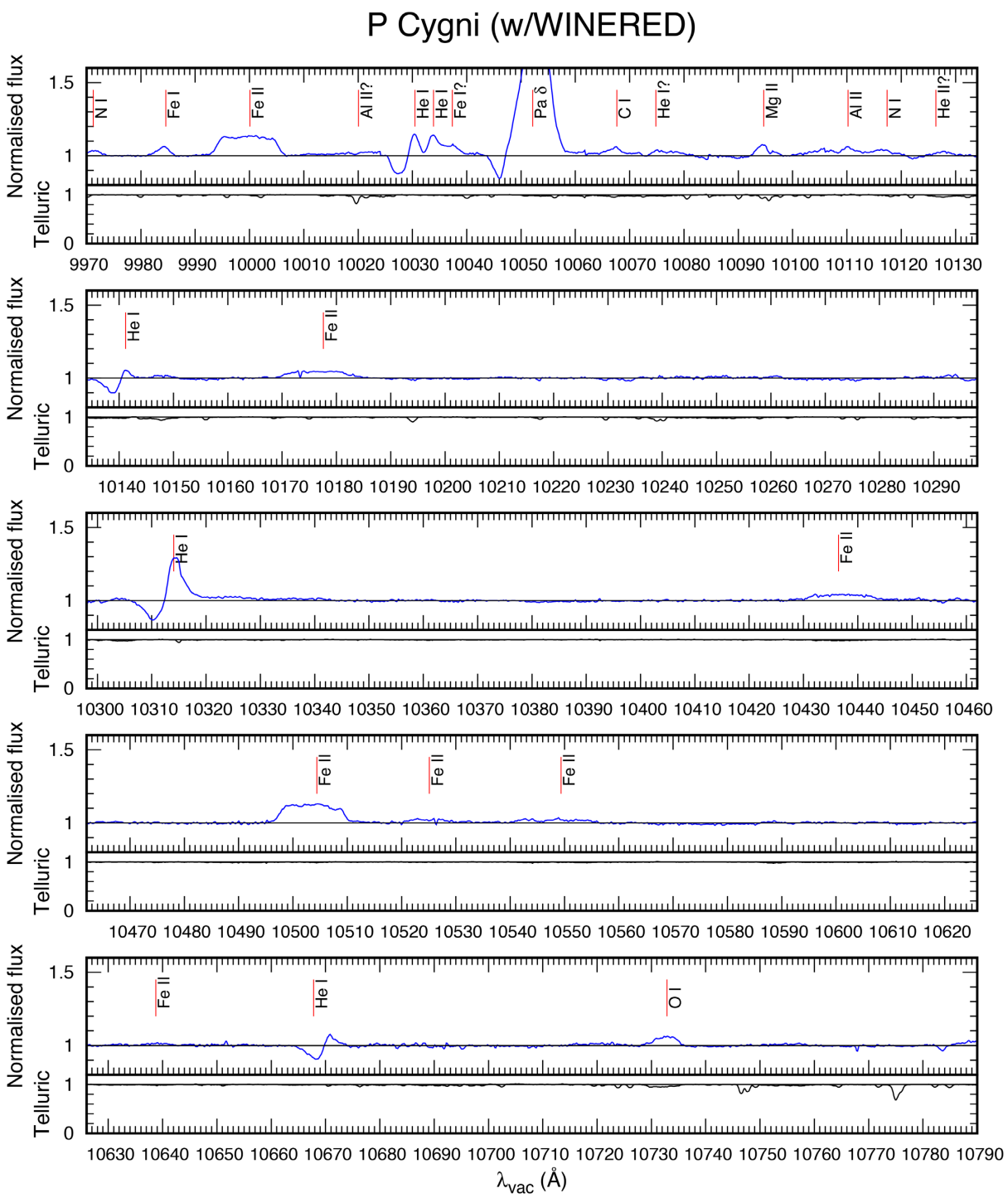

Figure 2 – *continued*

one-dimensional spectra for each spatial pixel between −15 and +15 arcsec and fitted the continuum spectra on both sides of the [Fe II] emission with a linear function. We then subtracted the best-fitting continuum spectra from the one-dimensional ones, and re-constructed the [Fe II] two-dimensional echelle image from all of the 52 one-dimensional spectra. In this reconstructed image, we binned each set of 9 pixels (=1.72 Å) along the wavelength axis in order to smear out stripe-like residuals on the continuum, which was generated as a side effect of pixelizing the rotated spectra on the detector array. As a result, the two velocity components are clearly separated into the two oval extensions in the spacio-velocity field, i.e. the 1600-AD outburst shell component with $v \simeq 140$ km s^{-1}

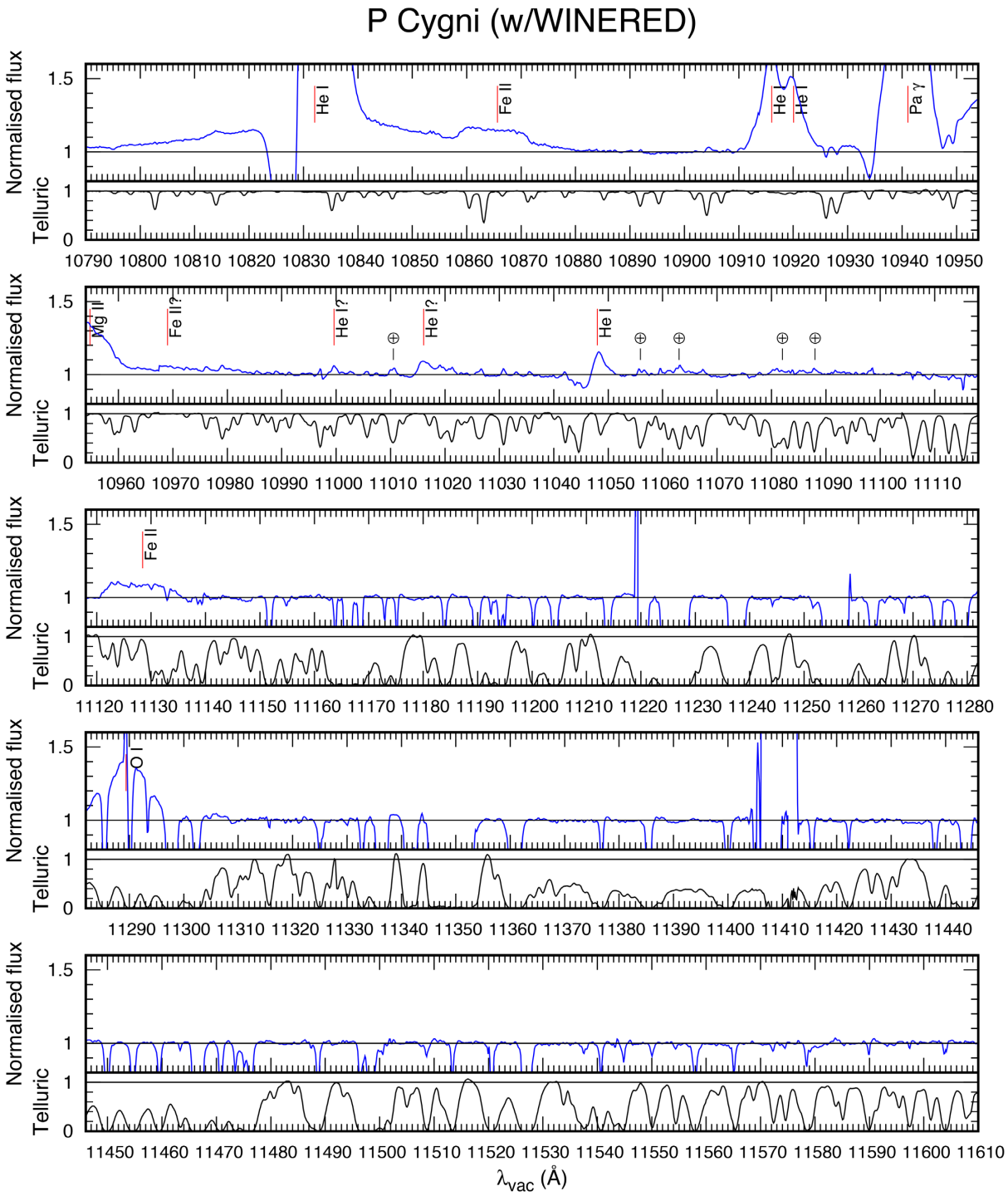

Figure 2 – *continued*

(green dashed line in the figure) and the 'double-peak' component with $v \simeq 220$ km s^{-1} (blue dotted), in the lower panel of Fig. 4.

We examined the spatial profiles of the *continuum-subtracted* echelle image to quantitatively estimate the spatial extent of the emission regions. The upper panel in Fig. 5 shows the [Fe II] spatial profile of the *continuum-subtracted* echelle image, thus pure emission line echelle image, at $v = 0$ km s^{-1}. We fitted the profile with three Gaussians: One represents the 'double-peak' component (blue dotted line in the figure) and the other two represent the blue- and redshifted components of the 1600-AD outburst shell (green dashed). The spatial width of the 'double-peak' component is 5.02 ± 0.03 arcsec at an FWHM, which is clearly broader than that of the adjacent continuum component, 4.1 ± 0.1 arcsec (grey dot-dot-dashed), which represents the seeing size because the continuum-emitting region is totally unresolved (Chesneau et al. 2000). This means that the [Fe II] emission-line region is intrinsically spatially extended. By comparing the two spatial profiles, the spatial extent even smaller than the seeing size can be examined (e.g. Takami et al. 2009). As-

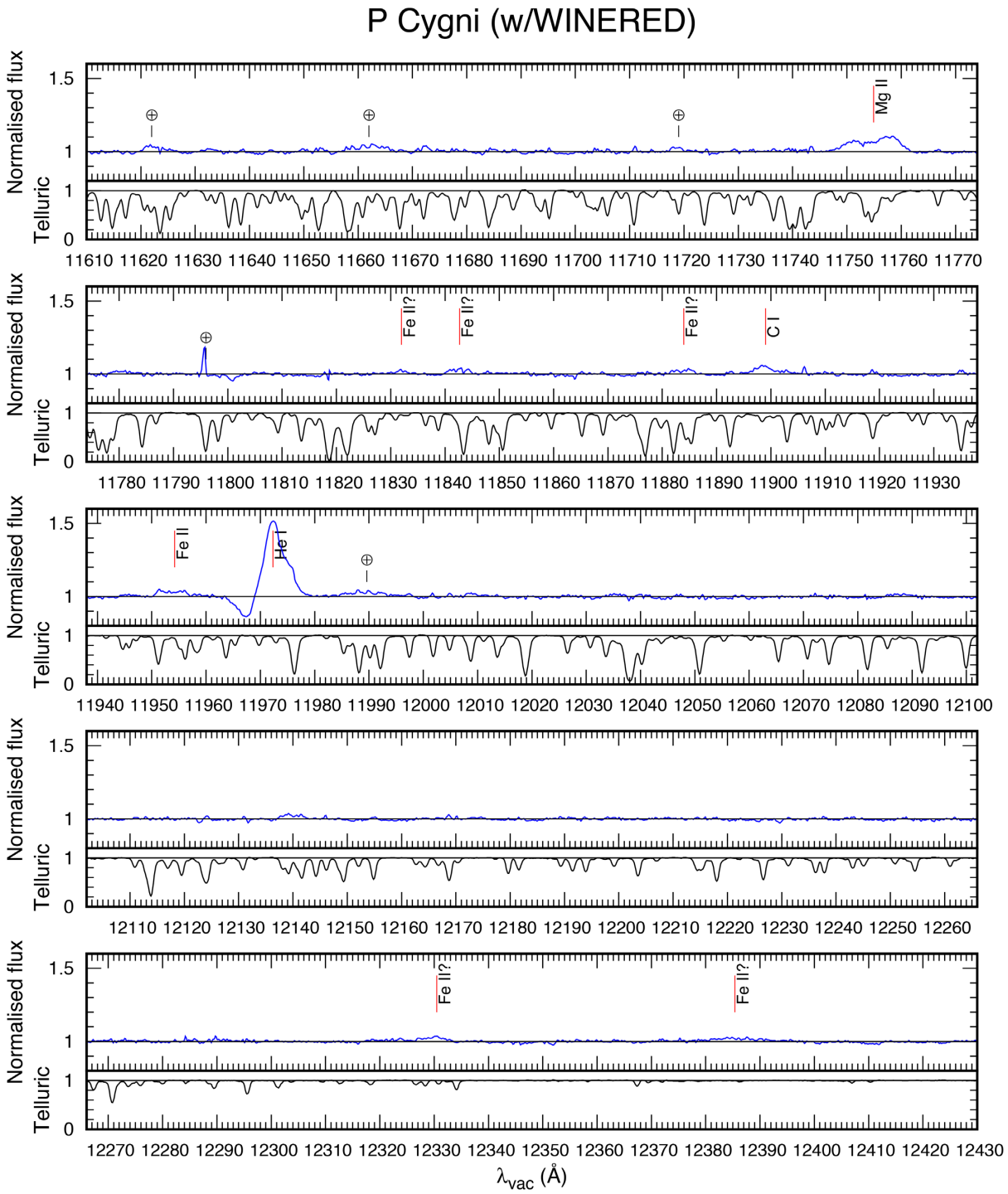

Figure 2 – *continued*

suming that the extension of the emission region can be modelled with Gaussians, the intrinsic FWHM of this component was estimated to be $\sqrt{(5.02 \pm 0.03\,\mathrm{arcsec})^2 - (4.1 \pm 0.1\,\mathrm{arcsec})^2} = 2.9 \pm 0.1$ arcsec, which corresponds to 4.9 ± 0.2 kau or $(1.39 \pm 0.05) \times 10^4\ R_*$ (see the dotted circle in Fig. 1).

For comparison, we made spatial profiles of He I λ12531 ('P Cygni' profile) and Fe II λ10504 ('rounded' profile) in the same way from the *continuum-subtracted* echelle image at $v = 0\,\mathrm{km\,s^{-1}}$, and plotted them in the medium and lower panels of Fig. 5. The observed, adjacent, and intrinsic FWHM of He I λ12531 are 4.2 ± 0.1, 4.2 ± 0.1, and 0 ± 0.6 arcsec, respectively, and those of Fe II λ10504 are 4.6 ± 0.2, 4.5 ± 0.2, and 1.0 ± 1.3 arcsec, respectively. This result shows that these lines are not extended spatially and are formed in a compact emission region close to the central star, as opposed to the [Fe II] lines.

In order to unambiguously separate the 'double-peak' component from those of the 1600-AD outburst shell, we made spatial profiles of the echelle image for all the Doppler velocity bins from −300

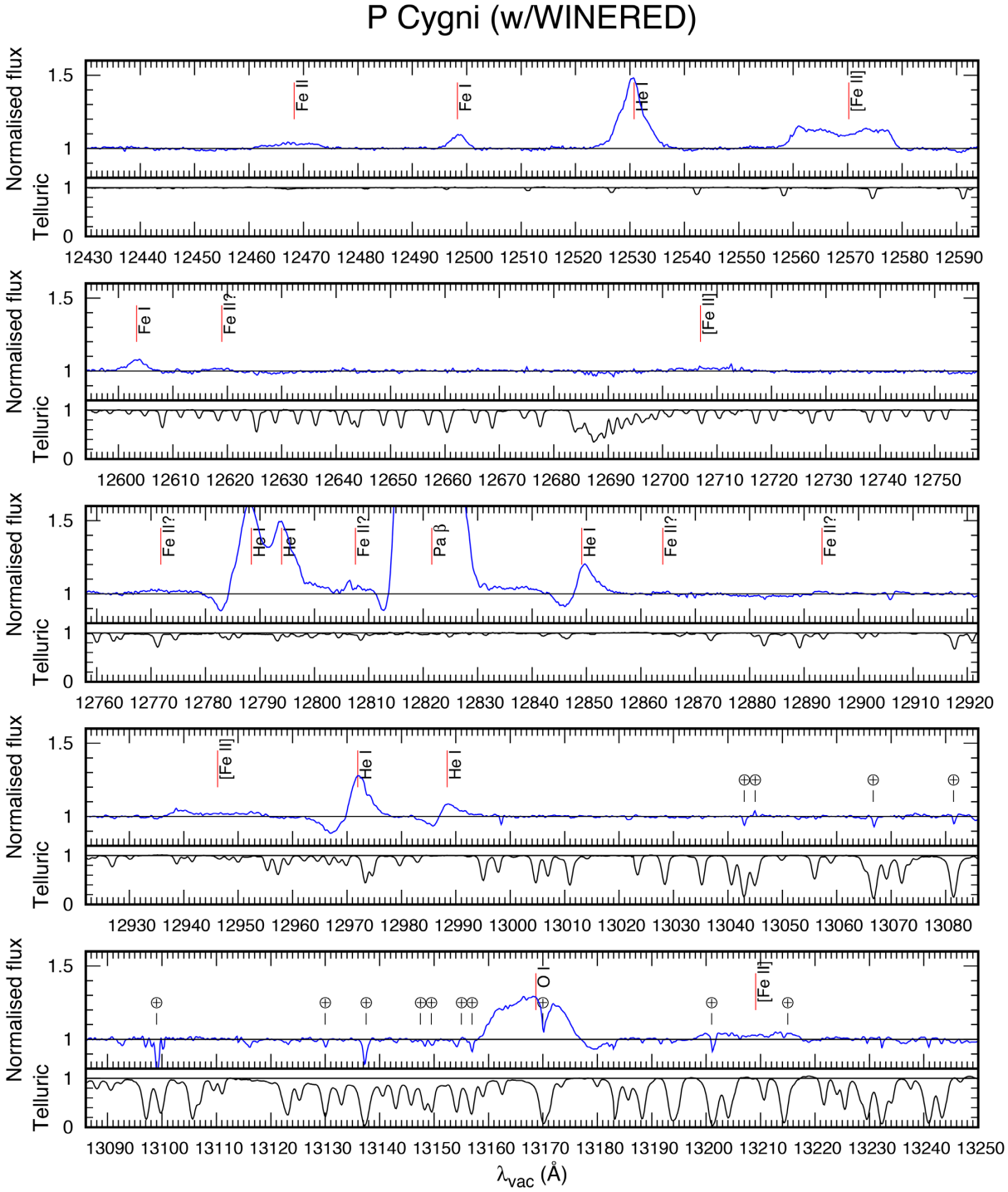

Figure 2 – *continued*

to +300 km s^{-1} with a 9 pixels (=41 km s^{-1}) step, and fitted all the components at $|v| \leq 140$ km s^{-1} and at $|v| > 140$ km s^{-1} with three and a single Gaussians, respectively (see Fig. 5c for the case of $|v| \leq 140$ km s^{-1}). The central Gaussian with the spatial offset of 0 arcsec indicates the 'double-peak' component, whereas the two side Gaussians at $|v| \leq -140$ km s^{-1} indicate the 1600-AD outburst shell. Next, we combined the fitted Gaussian profiles at all the Doppler velocity bins in the spacio-velocity plane to reconstruct the echelle image. Fig. 6 shows the reconstructed images, which encompass the 'double-peak' component (upper) and the 1600-AD outburst shell (lower). Fig. 7 shows the intrinsic FWHM of the 'double-peak' component, which is larger for smaller Doppler velocity. The red dashed line in Fig. 7 shows the model one when the emission region is spherical (FWHM $= 2.9$ arcsec$\sqrt{1-(v/220\,[\mathrm{km\,s^{-1}}])^2}$), which is consistent with the trend of the observation. Thus, the emission region is found to be (quasi-)spherical. Hereafter, we call the emission region of the 'double-peak' component as the 'extended emission region', in contrast to the 1600-AD outburst shell.

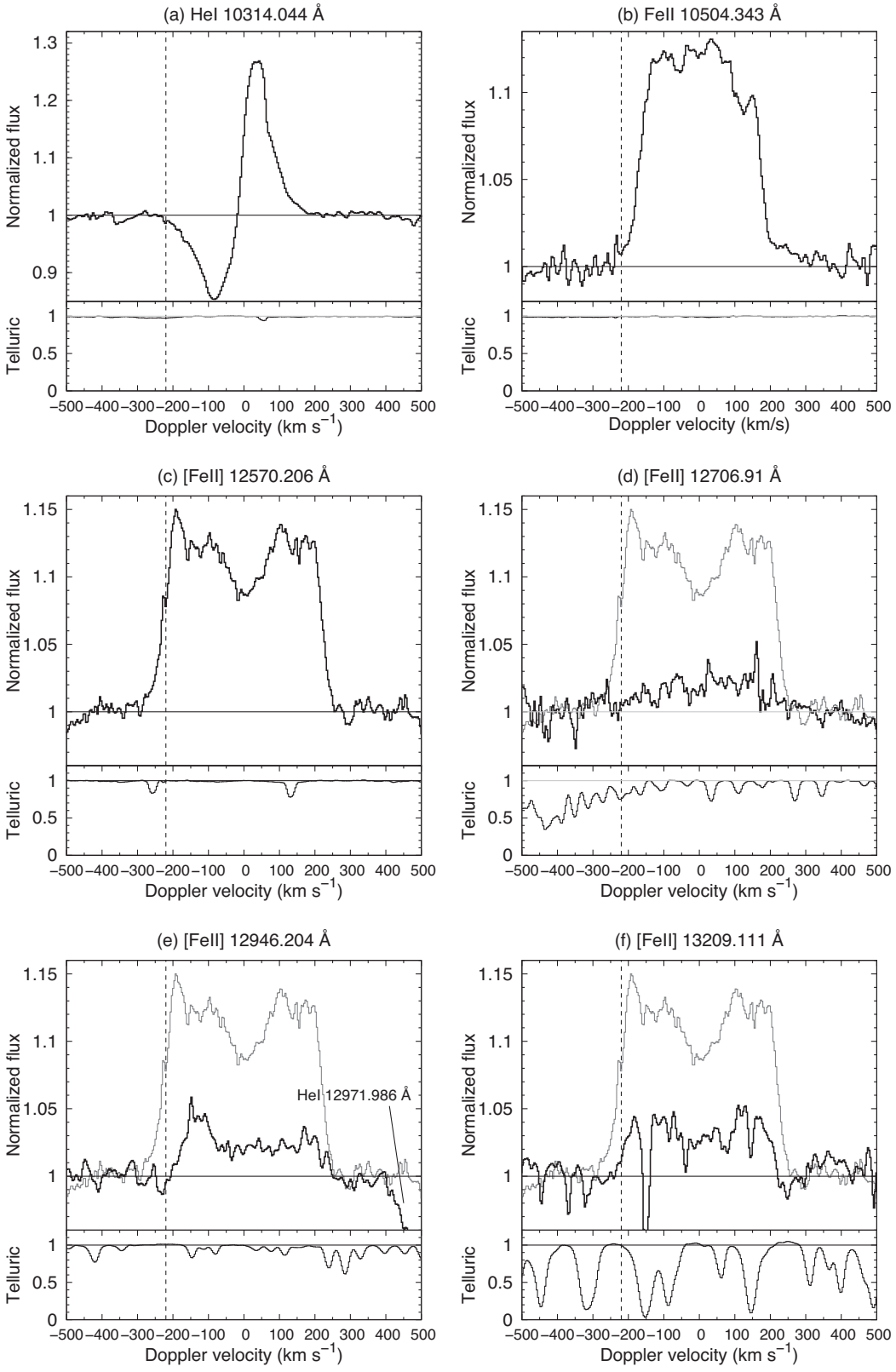

Figure 3. Velocity profiles after the systemic velocity is corrected. The profiles are normalized to fit the adjacent continuum to 1. The spectra are telluric corrected. The lower panels show profiles of the telluric standard star. The grey profiles superposed on the panels (d)–(f) show that of [FeII] λ12570, adopted from the panel (c), which is the strongest among all the observed [Fe II] lines. The vertical dashed lines show -220 km s^{-1}, which corresponds to the terminal velocity of the P Cygni profiles and the wind velocity of the [Fe II] profiles.

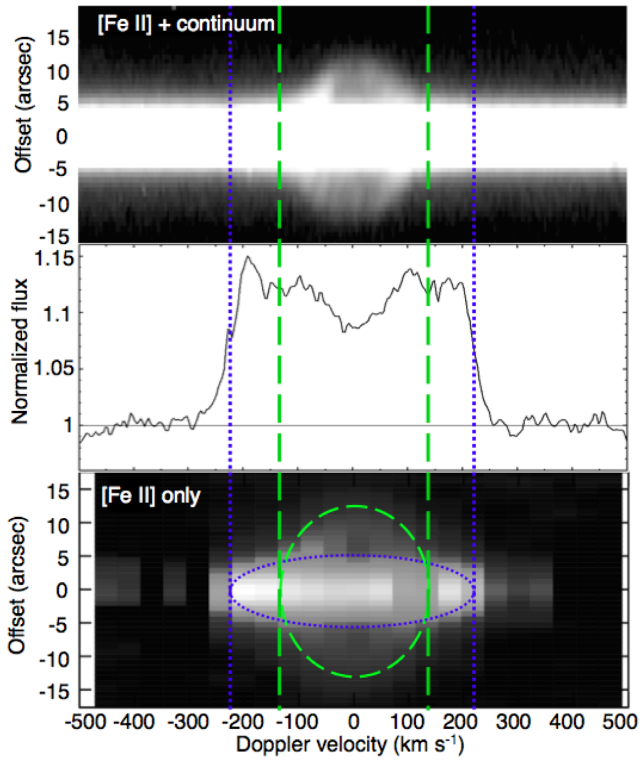

Figure 4. Upper panel: Echelle image around the [Fe II] λ12570 line. Middle panel: Velocity profile of the [Fe II] λ12570 line normalised to fit the adjacent continuum to 1, which was created using the data of −5 to +5 arcsec after telluric correction. Lower panel: Same image as the upper panel, but after the continuum subtraction. Note that two telluric absorption lines at $v \simeq -270$, +110 km s^{-1} cause slightly weaker signal at the corresponding binned elements. The blank areas at $v \simeq -370$ km s^{-1} and $v \gtrsim +360$ km s^{-1} have negative values after continuum subtractions due to statistical fluctuation. The green dashed and blue dotted lines indicate $v = \pm 140$ km s^{-1} and $v = \pm 220$ km s^{-1}, respectively.

This 'extended emission region' was, in fact, visible in SH06, though there was no mention about it in their paper. The top panel of fig. 4 in SH06 showed the intensity of [Fe II] λ12567 and λ16435 lines,[1] where the inner emission region appears in −4 to +4 arcsec, whereas the 1600-AD outburst shell component appeared in −10 to −7 arcsec and +8 to +11 arcsec. We concluded that its inner emission region is identical to the 'extended emission region' because the spatial extent of the regions is almost the same. Consequently, we managed to constrain the upper limit of the radius of the [Fe II] emission region, which has yet been unclear.

4 DISCUSSION

4.1 Origin of the [Fe II] 'double-peak' profile

When an emission line originates from an optically thin, spherically symmetric shell/flow with a constant velocity, the intensity per unit frequency bin is independent of frequency; as a result, the line shows a 'flat-topped' profile (Appenzeller, Oestreicher & Jankovics

[1]The observed wavelengths are used in SH06, whereas the vacuum wavelengths after the systemic velocity is corrected are used in this paper. Thus, the quoted wavelength values are slightly different between these two. For example, λ12567 in SH06 corresponds to λ12570 in this paper.

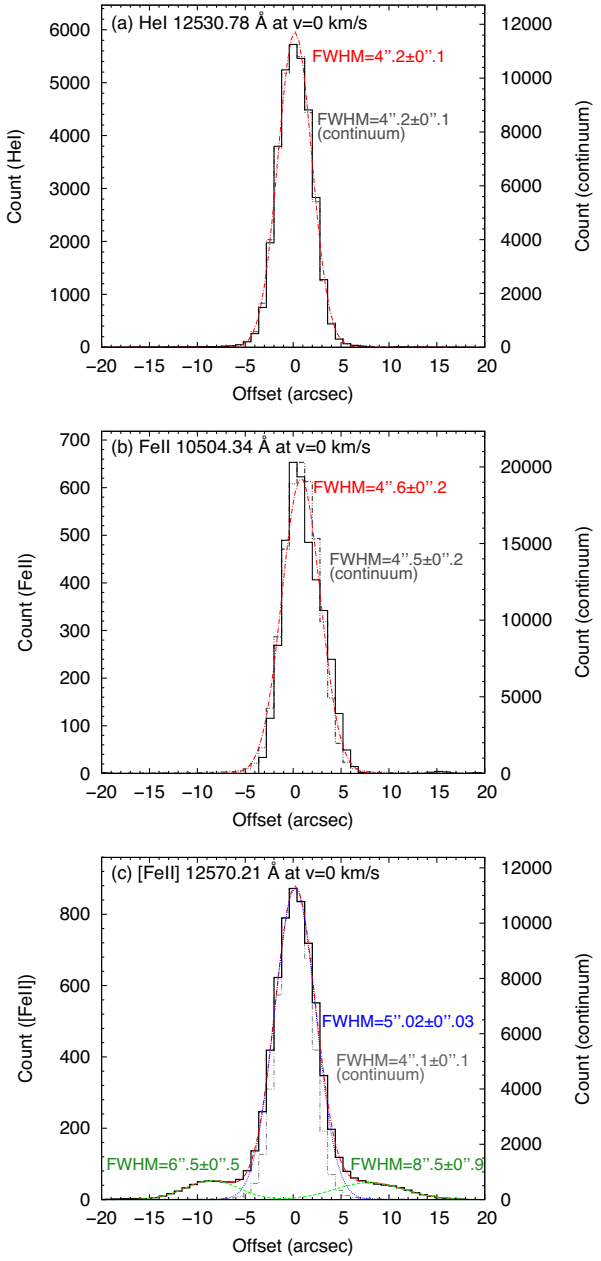

Figure 5. Spatial profiles of three kinds of emission lines after continuum-subtraction: the He I λ12530 line (a), Fe II λ10504 line (b), and [Fe II] λ12570 line (c) at $v = 0$ km s^{-1} (black solid). The grey dot–dot-dashed lines show the continuum component, whose scale in count is given on the right-hand axis in each panel. In the upper panel, the green dashed lines show the Gaussian-fitted model for the 1600-AD outburst shell component, the blue dotted line shows that for the 'double-peak' component, and the red dot–dashed line is the sum of the green and blue lines. In the medium and lower panels, the red dot–dashed lines show the Gaussian-fitted model.

1984; Shu 1991; Emerson 1999). The [Fe II] velocity profiles of P Cygni have been treated as flat-topped in literature so far, and thus the [Fe II] emission region of P Cygni has been considered as a compact and spherically symmetric layer expanding with a constant velocity (e.g. Israelyan & de Groot 1991; Stahl et al. 1991; Markova & de Groot 1997; Markova 2000; Kogure & Leung 2007). However, our observation with high-resolution NIR spectroscopy revealed that the [Fe II] lines of P Cygni have 'double-peak' profiles

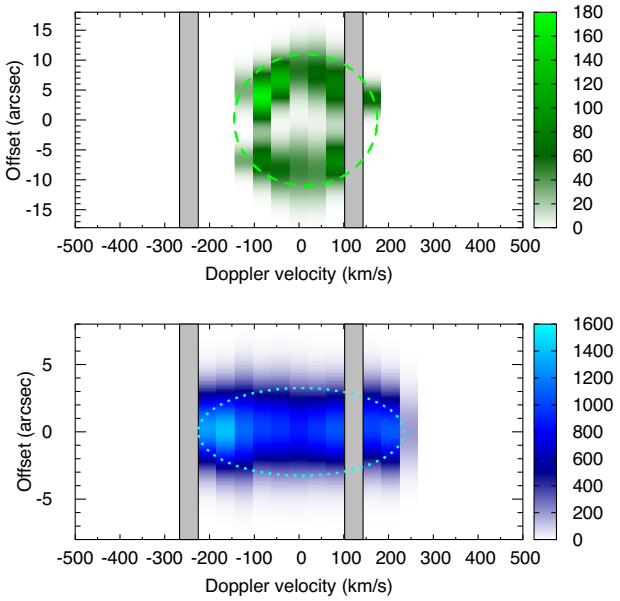

Figure 6. Reconstructed echelle images around the [Fe II] λ12570 line. Green-tinted image (upper) shows the 1600-AD outburst shell component, and blue-tinted image (lower) shows the extended emission region. The telluric absorption regions at $v \simeq -270, +110$ km s^{-1} are not displayed. The green-dashed and blue-dotted lines are same as Fig. 4.

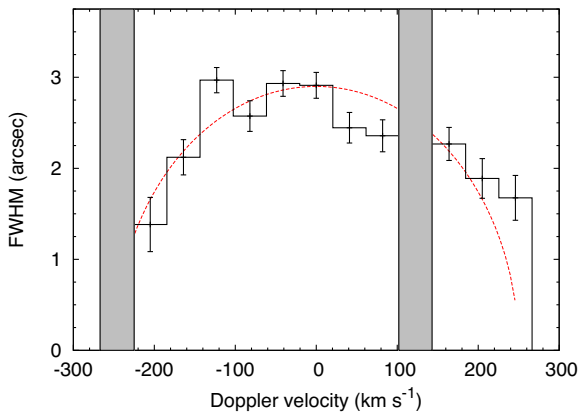

Figure 7. Intrinsic FWHM of the extended emission region. The telluric absorption regions at $v \simeq -270, +110$ km s^{-1} are masked. The red dashed line shows the model for spherical emission region.

(Section 3.1). Moreover, we found that the 'double-peak' emission region was spatially extended by 4.9 ± 0.2 kau (Section 3.2).

Is it plausible for the 'double-peak' profile to originate from the 'extended emission region'? In optical/IR spectroscopy, when a part of an optically thin spherically symmetric shell/flow with a constant velocity is masked by a slit of spectrograph, the intensity at the frequency corresponding to the radial velocity of the masked region becomes faint, and thus a part of 'flat-topped' velocity profile is scraped off (e.g. Chapter 9 of Shu 1991). Therefore, when the emission region is extended wider than the slit width and the extended component with a slow radial velocity is masked, the velocity profile becomes hollow at the centre. Assuming a spherical, homogeneous, and isotropic emission region, the model velocity profile can be calculated as a function of a diameter of the region. The blue-dotted line in Fig. 8 shows the model velocity profile of the emission region with a diameter of 2 arcsec, which is slightly larger than the slit width (1.6 arcsec). The expansion velocity of the model profile is set to be 220 km s^{-1}, and the instrumental resolution is fully taken into account. Residuals seen in the velocity range of −130 to +130 km s^{-1} (green-dashed) shows another clear double-peak profile, which is obviously a component of the 1600-AD outburst shell.

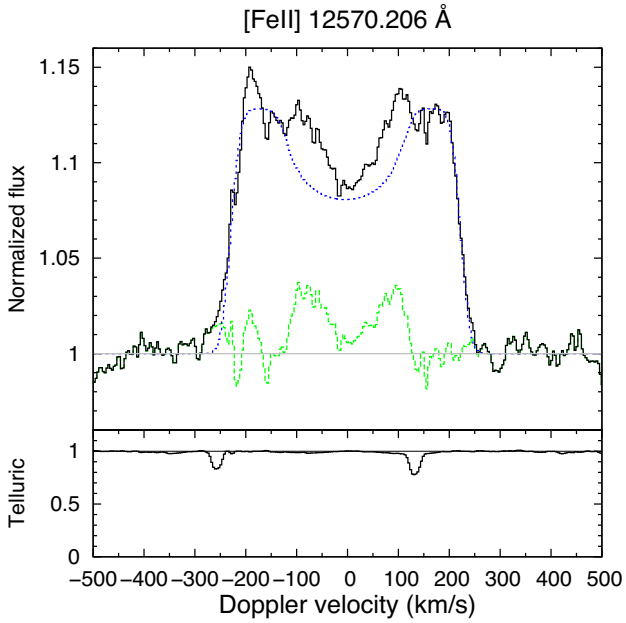

Figure 8. The observed velocity profile of [Fe II] λ12570 (black-solid; same as Fig. 3c) and the model one for the 'extended emission region' (blue-dotted; see the main text for the detail of the model). The green-dashed profile shows the residual component of the model fitting.

Indeed, the estimated diameter of the 'double-peak' emission region (as defined with FWHM $= 2.9 \pm 0.1$ arcsec; see Section 3.2) is similarly larger than the slit width (1.6 arcsec). The emission region may be regarded as a region with uniform density with a diameter of roughly 2 arcsec, but more accurate modelling should await slit-scanning data for acquiring information on radial density distribution. Consequently, the 'double-peak' velocity profile is expected, as was observed, when the emission region is partially masked with the slit of spectrograph. We must note that some intrinsic non-uniformity of the emission region can enhance or skew the spectral features.

4.2 Mass of the 'extended emission region'

Constraining the mass is essential to investigate the nature of the emission region. Under the assumption that the 'extended emission region' is spherically symmetric (Section 3.2), the total gas mass (M) is given by

$$M = \mu m_{\rm H} \frac{n_e}{f_{\rm H}} f \frac{4}{3} \pi \left(R_2^3 - R_1^3 \right), \quad (1)$$

where μ is the mean molecular weight, $m_{\rm H}$ is the mass of hydrogen atom, $n_{\rm e}$ is the number density of electron, $f_{\rm H}$ is the hydrogen ionization fraction, f is the filling factor, and R_2 and R_1 are the outer and inner radii of the emission region, respectively (SH06). The mean molecular weight μ is assumed to be 2.2. $f_{\rm H}$ in the 1600-AD outburst shell is calculated to be 0.86, using the line ratio [N II]/[N I] in SH06. In the 'extended emission region', hydrogen atoms should be almost

fully ionized because they are much closer to the central star than the 1600-AD outburst shell. Therefore, we treated f_H in the 'extended emission region' as unity. The outer radius R_2 of the 'extended emission region' is 1.45 arcsec. The inner radius R_1 must be small, given the spatial profile of the [Fe II] λ12570 line (Fig. 5c) shows no apparent dip near the central star. Here, we set $R_1 = 0$. Estimating f in the 'extended emission region' is difficult because our observation could not spatially resolve its substructure in detail. We assumed that f is similar to that of the 1600-AD outburst shell in SH06, and adopt $f = 0.2 \pm 0.1$. n_e can be calculated based on the ratios of the diagnostic [Fe II] lines, λ12567/λ16435 and λ15535/λ16435 (SH06; see the second footnote for the notations). In fig. 4 of SH06, we read λ15535/λ16435 as 0.16 in the 'extended emission region' and as 0.1 in the 1600-AD outburst shell. In SH06, λ12567/λ16435 was 1.3 throughout the regions, and thus λ15535/λ12567 is calculated to be 0.12 and 0.08 in the 'extended emission region' and the 1600-AD outburst shell, respectively. Comparing the λ15535/λ12567 ratios with the values in fig. 3 of Nussbaumer & Storey (1988), we can estimate the respective electron densities to be $n_e = 10000\,\mathrm{cm}^{-3}$ in the 'extended emission region' and $6000\,\mathrm{cm}^{-3}$ in the 1600-AD outburst shell. The n_e value hardly depends on the electron temperature in this range. With all the needed parameters (Table 2), we derived the gas mass in the 'extended emission region' to be $(8 \pm 4) \times 10^{-4}\,\mathrm{M}_\odot$. This value is about 0.5 per cent of that in the 1600-AD outburst shell, $M = 0.16 \pm 0.08\,\mathrm{M}_\odot$. The mass-loss rate with a constant stellar wind of P Cygni is $3 \times 10^{-5}\mathrm{M}_\odot\,\mathrm{yr}^{-1}$ (Najarro et al. 1997a,b); accordingly, the 'extended emission region' contains gas of the constant stellar wind within 30 ± 15 yr. This value is consistent with a dynamical age, $R/\dot{R} = 2.45\,\mathrm{kau}/220\ \mathrm{km\ s}^{-1} \sim 50\,\mathrm{yr}$, which means that the total mass of this region can be explained by the steady stellar wind. As a result, the 'extended emission region' is not considered to be a remnant shell of an eruption but a stellar wind region.

4.3 [Fe II] excitation

The bright IR [Fe II] emission is detected in all the observed LBVs with NIR spectroscopy (Smith 2002a). For example, Smith (2006) showed the [Fe II] λ16435 spacio-velocity map of η Carinae and clearly indicated the two distinct emission regions within the nebulae; one is the thicker skin extended inside of the H_2 shell and consistent with the 'Homunculus', and the other is the inner region and consistent with the 'Little Homunculus' (Ishibashi et al. 2003; Smith 2005).

The origin of the forbidden lines of LBV nebulae are not completely clear (Smith 2002a, 2012). On one hand, the shocked stellar wind interacted with the ambient medium radiates the forbidden lines: Smith (2002a) reported that the NIR [Fe II] lines are good probes of shock-excited events such as LBV eruptions. If the 'extended emission region' of P Cygni is heated by shock, its origin could be an episodic and relatively strong wind that occasionally happens due to stellar fluctuations. On the other hand, the forbidden lines may simply be radiatively excited (Smith 2006): Smith & Ferland (2007) suggested that, compared with shock heating, radiative heating dominates the energy balance in the Homunculus of η Carinae by two orders of magnitude. If the 'extended emission region' of P Cygni is radiatively heated, what we see in the region is a simply steady stellar wind with less number density and then is more extended than the compact stellar wind region traced by other lines. As a result, both scenarios are consistent with the statement that the 'extended emission region' of P Cygni traces a stellar wind, not an eruption.

4.4 Origin of the 'extended emission region'

The expansion velocity of the 'extended emission region' ($\sim$220 km s^{-1}) is consistent with the terminal velocity seen in the P Cygni profile (see the vertical lines in Fig. 3). This implies that the 'extended emission region' traces the outer wind after being accelerated and reaching the terminal velocity. The expansion velocity of this region is faster than that of the 1600-AD outburst shell ($\sim$140 km s^{-1}), suggesting that this region overtakes the outer shell, produces a reverse shock, and emits the [Fe II] emission. A numerical simulation in Dwarkadas & Balick (1998) shows that such a reverse shock emerges in the LBV nebulae (assuming η Carinae), and its radius can be several times smaller than the outer shell, like this 'extended emission region'. Consequently, we propose that the 'extended emission region' traces the reverse shock region due to the stellar wind overtaking inside of the outburst shell.

Both the 1600-AD outburst shell region and the 'extended emission region' show some brightness asymmetry in our data, although we have discussed them with a spherically symmetric geometry so far. In the upper plot of Fig. 6, a bright emission was visible at the northern blueshifted part in the 1600-AD outburst shell.[2] In the lower panel of Fig. 6, the blueshifted part of the 'extended emission region' is found to be brighter than the other areas. Because the 1600-AD outburst shell does not have velocity components at $v > 140$ km s^{-1}, this bright spot of the 'extended emission region' is free from contamination of the shell. As a result, the two regions may share the similar asymmetry although they are spatially separated. This similarity also supports the reverse shock scenario; the denser region in the 1600-AD shell naturally causes stronger emission in the shock as the wind overtakes the inside of the shell.

The extended [Fe II] emission are also observed in the stellar wind region of η Carinae. Smith et al. (2004) found a UV excess emission region at 0.1−0.6 arcsec from the central star of η Carinae, which emanates from the outer parts of the stellar wind region. Hillier et al. (2006) detected a UV [Fe II] emission line from the UV region, 0.2 from the central star. This [Fe II] emission region in η Carinae is similar to the 'extended emission region' in P Cygni; both are spatially extended around the central star and considered to be the outer parts of the stellar wind region. Moreover, their sizes are not so much different (0.2–1.4 kau for η Carinae and 4.9 kau for P Cygni), and may scale with the luminosity of the central source. Therefore, such extended [Fe II] emission regions could be a common structure in LBV nebulae.

Structure of the P Cygni nebulae we propose in this paper is as follows. The inner region of the wind ($\lesssim 100\,R_*$) is traced by the metal permitted lines ($v = 180$ km s^{-1}). The wind is accelerated by the radiation of the central star and reaches the terminal velocity at $\sim 300\,R_*$ (Lamers et al. 1985), which is traced by the P Cygni profile of H- and He emission lines ($v = 220$ km s^{-1}). The wind velocity exceeds the expansion velocity of the 1600-AD outburst shell ($v = 140$ km s^{-1}), so that the reverse shock emerges when the wind overtakes the shell, which produces the [Fe II] 'extended emission region' we have found in this paper ($v = 220$ km s^{-1}). The radius and total gas mass of the shock region are about 15 per cent and 0.5 per cent of those of the 1600-AD outburst shell. A promising way to study details of this newly found region would be to spatially resolve it (within 3 arcsec from the central star) with adaptive-optics observations of the [FeII] lines.

[2]This feature is also seen in fig. 5 of SH06 though the slit positions were not identical.

Table 2. Parameters of the two [Fe II] emission regions.

		1600-AD outburst shell[a]	Extended emission region
Mean molecular weight	μ	2.2	
Number density of electron	n_e (cm^{-3})	6000	10000
Hydrogen ionization fraction	$f_{\rm H}$	0.86	1
Filling factor	f	0.2 ± 0.1	
Outer radius	R_2 (arcsec)	9.7	1.45
Inner radius	R_1 (arcsec)	7.8	0
Total gas mass	M	$\simeq 0.16 \pm 0.08\,{\rm M}_\odot$	$\simeq (8 \pm 4) \times 10^{-4}\,{\rm M}_\odot$

[a]The values in this column are adopted from SH06.

ACKNOWLEDGEMENTS

We are grateful to the staff of Koyama Astronomical Observatory for their support during our observation. This study is financially supported by KAKENHI (16684001) Grant-in-Aid for Young Scientists (A), KAKENHI (20340042) Grant-in-Aid for Scientific Research (B), KAKENHI (26287028) Grant-in-Aid for Scientific Research (B), KAKENHI (21840052) Grant-in-Aid for Young Scientists (Start-up), and JSPS, MEXT – Supported programme for the Strategic Research Foundation at Private Universities, 2008–2012, S0801061. This work has made use of the VALD data base, operated at Uppsala University, the Institute of Astronomy RAS in Moscow, and the University of Vienna.

REFERENCES

Appenzeller I., Oestreicher R., Jankovics I., 1984, A&A, 141, 108
Arcidiacono C. et al., 2014, MNRAS, 443, 1142
Artigau É., Martin J. C., Humphreys R. M., Davidson K., Chesneau O., Smith N., 2011, AJ, 141, 202
Barlow M. J., Drew J. E., Meaburn J., Massey R. M., 1994, MNRAS, 268, L29
Chesneau O. et al., 2000, A&AS, 144, 523
Clark J. S., Arkharov A., Larionov V., Ritchie B., Crowther P., Najarro F., 2011, Bull. Soc. R. Sci. Liege, 80, 361
Dwarkadas V. V., Balick B., 1998, AJ, 116, 829
Emerson D., 1999, Interpreting Astronomical Spectra, Wiley-VCH, New York
Groh J. H., Damineli A., Jablonski F., 2007, A&A, 465, 993
Gvaramadze V. V. et al., 2012, MNRAS, 421, 3325
Hamann F., Depoy D. L., Johansson S., Elias J., 1994, ApJ, 422, 626
Hartigan P., Raymond J., Pierson R., 2004, ApJ, 614, L69
Hillier D. J. et al., 2006, ApJ, 642, 1098
Humphreys R. M., Davidson K., Smith N., 1999, PASP, 111, 1124
Ikeda Y. et al., 2016, Proc. SPIE, 9908, 99085Z
Ishibashi K. et al., 2003, AJ, 125, 3222
Israelyan G. L., de Groot M., 1991, Astrophysics, 34, 171
Kogure T., Leung K.-C., eds., 2007, The Astrophysics of Emission-Line Stars Astrophysics and Space Science Library, Vol. 342. Springer-Verlag, New York, p. 1.
Kupka F., Piskunov N., Ryabchikova T. A., Stempels H. C., Weiss W. W., 1999, A&AS, 138, 119
Lamers H. J. G. L. M., 1986, in De Loore C. W. H., Willis A. J., Laskarides P., eds, Proc. IAU Symp. 116, Luminous Stars and Associations in Galaxies. Reidel, Dordrecht, p. 157
Lamers H. J. G. L. M., de Groot M., Cassatella A., 1983, A&A, 128, 299
Lamers H. J. G. L. M., Korevaar P., Cassatella A., 1985, A&A, 149, 29
Langer N., Hamann W.-R., Lennon M., Najarro F., Pauldrach A. W. A., Puls J., 1994, A&A, 290
Lee H.-G., Moon D.-S., Koo B.-C., Lee J.-J., Matthews K., 2009, ApJ, 691, 1042
Markova N., 2000, A&AS, 144, 391
Markova N., de Groot M., 1997, A&A, 326, 1111
Meaburn J., 2001, in de Groot M., Sterken C., eds, ASP Conf. Ser. Vol. 233, P Cygni 2000: 400 Years of Progress. Astron. Soc. Pac., San Francisco. p. 253
Meaburn J., Lopez J. A., Barlow M. J., Drew J. E., 1996, MNRAS, 283, L69
Meaburn J., O'connor J. A., López J. A., Bryce M., Redman M. P., Noriega-Crespo A., 2000, MNRAS, 318, 561
Meynet G., Georgy C., Hirschi R., Maeder A., Massey P., Przybilla N., Nieva M.-F., 2011, Bull. Soc. R. Sci. Liege, 80, 266
Najarro F., Kudritzki R.-P., Hillier D. J., Lamers H. J. G. L. M., Voors R. H. M., Morris P. W., Waters L. B. F. M., 1997a, in Nota A., Lamers H., eds, ASP Conf. Ser. Vol. 120, Luminous Blue Variables: Massive Stars in Transition. Astron. Soc. Pac., San Francisco, p. 105
Najarro F., Hillier D. J., Stahl O., 1997b, A&A, 326, 1117
Nussbaumer H., Storey P. J., 1988, A&A, 193, 327
Rossi C., Muratorio G., Viotti R. F., 2001, in de Groot M., Sterken C., eds, ASP Conf. Ser. Vol. 233, P Cygni 2000: 400 Years of Progress. Astron. Soc. Pac., San Francisco, p. 105
Shinn J.-H. et al., 2013, ApJ, 777, 45
Shu F. H., 1991, The Physics of Astrophysics. Volume 1: Radiation, University Science Books, Mill Valley, CA, USA
Smith N., 2001, in de Groot M., Sterken C., eds, ASP Conf. Ser. Vol. 233, P Cygni 2000: 400 Years of Progress. Astron. Soc. Pac., San Francisco, p. 125
Smith N., 2002a, MNRAS, 336, L22
Smith N., 2002b, MNRAS, 337, 1252
Smith N., 2005, MNRAS, 357, 1330
Smith N., 2006, ApJ, 644, 1151
Smith N., 2012, in Davidson K., Humphreys R. M., eds, Astrophysics and Space Science Library, Eta Carinae and the Supernova Impostors, vol 384, Splinger, Berlin, p. 145
Smith N., 2014, ARA&A, 52, 487
Smith N., Ferland G. J., 2007, ApJ, 655, 911
Smith N., Hartigan P., 2006, ApJ, 638, 1045 (SH06)
Smith N. et al., 2004, ApJ, 605, 405
Smith N., Li W., Silverman J. M., Ganeshalingam M., Filippenko A. V., 2011, MNRAS, 415, 773
Stahl O., Mandel H., Szeifert T., Wolf B., Zhao F., 1991, A&A, 244, 467
Stahl O., Mandel H., Wolf B., Gaeng T., Kaufer A., Kneer R., Szeifert T., Zhao F., 1993, A&AS, 99, 167
Takami H. et al., 2009, PASJ, 61, 623
Weis K., 2011, Bull. Soc. R. Sci. Liege, 80, 440
Yoshikawa T., Ikeda Y., Fujishiro N., Ichizawa S., Arai A., Isogai M., Yonehara A., Kawakita H., 2012, Proc. SPIE, 8444, p. 84446G

This paper has been typeset from a TEX/LATEX file prepared by the author.